Heliyon 10 (2024) e37689

Contents lists available at ScienceDirect

Heliyon

journal homepage: www.cell.com/heliyon

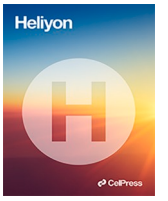

Research article

Synergistic effects of rare-earth ions (Ho, Yb) doping on the photo-catalytic efficacy of V_2O_5 for removal of pollutants from industrial waste water

M.M. Uddin [a,*], M.Z. Hossain [a], M.H. Kabir [a,b], S. Ghosh [c], M.H. Haque [a], M.M. Hossain [a], M.A. Ali [a], Md Akhtaruzzaman [d,**], Abdulaziz M. Alanazi [d], S. Mondal [e], J. Chowdhury [c], D. Karmakar [f], D. Jana [f]

[a] Department of Physics, Chittagong University of Engineering and Technology (CUET), Chattogram, 4349, Bangladesh
[b] Department of Materials Science & Engineering, Chittagong University of Engineering and Technology (CUET), Chattogram, 4349, Bangladesh
[c] Department of Physics, Jadavpur University, 188, Raja S.C. Mallick Road, Kolkata, 700032, India
[d] Department of Chemistry, Faculty of Science, The Islamic University of Madinah, Saudi Arabia
[e] Department of Physics, Sidho-Kanho-Birsha University, Purulia, 723104, India
[f] Department of Physics, University of Calcutta, 92 A P C Road, Kolkata, 700009, West Bengal, India

ARTICLE INFO

Keywords:
Synergistic effects
V_2O_5
Hydrothermal
Methylene blue
Rare-earth
Co-doped
DFT calculations

ABSTRACT

The co-doping of vanadium pentoxide (V_2O_5) with rare-earth (RE) elements, namely 1.5 % holmium (Ho) and 1.5 % ytterbium (Yb) has been conducted using an eco-friendly, straightforward hydrothermal approach to assess the combined effects on structural, optical, and photocatalytic properties. The application of the density functional theory (DFT) approach effectively examined the impact of RE ions on the photocatalytic efficiency of co-doped V_2O_5. The stable orthorhombic crystal structure of co-doped V_2O_5 has been confirmed using DFT and X-ray diffraction without a secondary phase. It appears that homogeneous nucleation occurs while heterogeneous nucleation slows down in co-doped samples, as evidenced by the larger crystallite sizes in co-doped samples compared to doped ones. It means a result, the co-doped samples exhibit photodegrades more quickly and have a higher rate constant than the doped samples. This is because they have less dislocation density (4.26×10^{-3} nm^{-2}) and internal micro-strain (4.93×10^{-3}). The bandgap and degradation efficiency are determined by the UV–vis spectroscopy and found to be 2.33 eV and 95 %, respectively, at the optimal pH of 7 in the visible range. The co-doped sample has a rate constant of 24×10^{-3} min^{-1}, which is the highest in the RE-doped V_2O_5 system. This is a good reason to think of co-doped V_2O_5 as a possible catalyst.

1. Introduction

Water pollution, one of the world's biggest problems, poses a physical, chemical, and biological hazard to human health and the

* Corresponding author.
** Corresponding author.
E-mail addresses: mohi@cuet.ac.bd (M.M. Uddin), makhtar@iu.edu.sa (M. Akhtaruzzaman).

https://doi.org/10.1016/j.heliyon.2024.e37689
Received 9 May 2024; Received in revised form 5 September 2024; Accepted 9 September 2024
Available online 10 September 2024

environment. The main sources of pollution are often chemicals suspended or dissolved in the water. Common pollutants include pathogens (fungi, bacteria, and viruses), inorganic compounds like heavy metals, plastics, noxious gases like NO_x, SO_x, CO, and NH_3, volatile organic compounds, organic dyes, insecticides, herbicides, pesticides, disinfection byproducts, detergents, and surfactants [1]. Photocatalytic materials release free radicals since they are exposed to room temperature sunlight and facilitate the breakdown of pollutants. This makes photocatalytic materials one of the most effective approaches to address environmental and water pollution [2]. Moreover, the photocatalysis method involves the use of visible or ultraviolet (UV) light to activate a catalyst, often a semiconductor oxide, which speeds up the rate of chemical processes (oxidation or reduction) [1,3]. The photocatalytic activity of a material is based on its crystal phase, band gap energy, unique shape, surface-to-volume ratio, and other properties that make it unique [4]. Metal oxides are often used as photocatalysts because they are very stable in a wide range of conditions, don't harm living things, and can create charge carriers when exposed to enough light energy. They break down solar energy systems, various harmful substances, and even split water into hydrogen and oxygen [5–9].

Vanadium produces a series of oxides, including VO, V_2O_3, VO_2, and V_2O_5, like other transitional metals [4,10,11]. The most significant and stable component of this series is V_2O_5. Because its d-orbitals are only partly filled, vanadium has a number of connected structural and electrical properties in vanadium oxides and related catalysts. There are several different oxidation states in which vanadium atoms can occur. Consequently, oxidation or reduction can be used to transform oxides with varying stoichiometry. Vanadium is the transition metal V_2O_5, an oxyanion with a band gap ranging from 2.3 eV to 2.8 eV [12,13] and melting and boiling points of approximately 936 K and 2020 K, respectively. Because of promise for usage as a photocatalyst under visible light because it has a high specific surface area and high surface acidity [13–16]. Powder form [16] rewards V_2O_5 for its photocatalytic ability, breaking down acetone [17], hydrocarbons [18], methylene blue [19], and other substances. When catalysts based on vanadium oxide are used, the catalytic reaction for the anisotropy of chemical bonds in the V_2O_5 crystal lattice is structurally sensitive [20]. The V_2O_5 is a narrow band gap, it may absorbs visible light that leads to the creation of energetic redox centers [21] and electron-hole pairs [22] and enhances photodegradation efficiency. Nevertheless, V_2O_5's photodegradation effectiveness is limited due to its reduced specific surface area and the rapid recombination of photoinduced charge carriers [21].

One popular method for reducing or solving the rapid recombination issue is cation doping. Several reports have focused regrading on cation doping to V_2O_5 nanoparticles and categories in three main categories: metals such as Na, Mg, and Al [11,23,24], transition metals like Titanium, Manganese, Iron, Cobalt, Nickel, Copper, Zinc, Zirconium, Molybdenum, Yttrium and Tin [25–34], and lanthanum series like Yttrium, Lanthanum, Cerium, Neodymium, Gallium, and Gadolinium [35–40]. Interestingly, most of them report related to storage capacity. Researchers try to improve the photocatalytic behavior of doped V_2O_5 by adding main group metals (Al^{3+}) [11] and transition metals [30,40], but in the first case, electron sinks, and in the latter case, altering surface morphology improves ability of oxidizing along with active sites results fail to enhance photocatalytic efficiency.

RE elements can simply target organic dyes or pollutants by creating complex compounds due to their partially filled 4*f* and empty 5*d* orbitals and altering bandgap to match for degradation [36,38,41]. Because of the way 4*f* orbitals raises oxygen vacancies, this has recently become a popular way to boost photocatalytic activity. This makes it easier for photo-generated electrons to get stuck in the newly formed vacancies, which slows down the rate at which the electron-hole pair recombines [39]. Recently, researchers doped holmium (Ho) and ytterbium (Yb) into V_2O_5 nanoparticles using the hydrothermal technique, reporting degradation efficiencies of 93

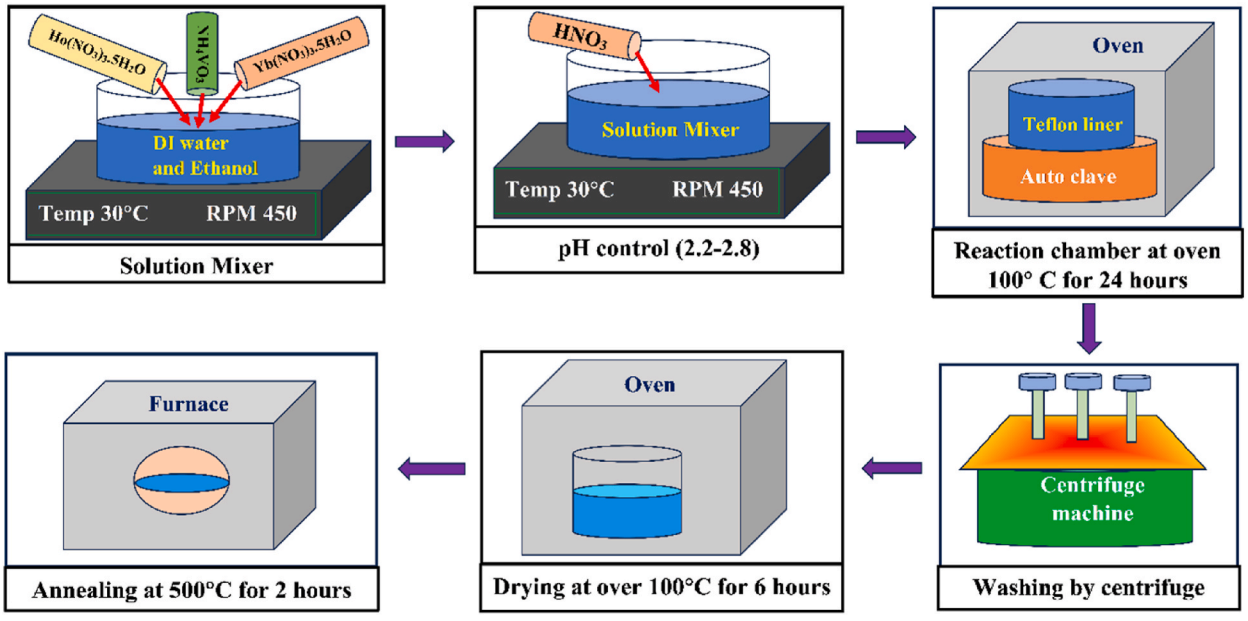

Fig. 1. Various steps of preparation of 1.5%Ho - 1.5%Yb co-doped into V_2O_5 (HYVO).

% and 95 % for 3 mol% within 2 h, respectively [42]. A lot of research needs to be done on the photocatalytic activity of V_2O_5, especially on how the Ho and Yb RE ions doping into V_2O_5 work together. Only then can V_2O_5 be suggested as a possible catalyst for breaking down pollutants or dyes. Therefore, the initiative has been taken to notice the impact of synergetic doping on the physical properties of bare V_2O_5, using both experimental and DFT calculations. The optical properties have also been detail studied to understand its dye degradation efficiency.

2. Experimental and computational approach

Ammonium metavanadate (NH_4VO_3), Holmium(III) nitrate pentahydrate ($Ho(NO_3)_3{\cdot}5H_2O$), and Ytterbium(III) nitrate pentahydrate ($Yb(NO_3)_3{\cdot}5H_2O$) were utilized. Sigma Aldrich (Germany) supplied the ingredients. We used simple hydrothermal synthesis to create the bare, Ho-doped, and Yb-doped V_2O_5. As seen in Fig. 1, the specific steps involved in the synthesis of bare V_2O_5 are explained elsewhere [42,43]. The synthesis technique for Ho and Yb-doped V_2O_5 involves dissolving ammonium metavanadate in ethanol and de-ionized (DI) water in an equal ratio to achieve a 1M concentration. A 1.5 mol% Ho/Yb precursor added to the solution as a doping ingredient. Next, 10 wt% nitrite acid addition to create an acidic medium while maintaining a specific pH level. This solution then agitated for an hour at room temperature, then placed it in a Teflon-coated hydrothermal autoclave and heated it to 100 °C for 24 h. The products centrifuged more than few times by DI water, ethanol, and then dried using oven for 6 h. Ultimately, the crystallinity enhanced of product by annealing it for 2 h at 500 °C. An XRD BRUKER AXS D8 advanced diffractometer with Cu-Kα radiation ($\lambda = 1.5406$ Å) used to study the structure of the material using the X-ray diffraction (XRD) method. Rietveld refinement has also been done to determine the precise atomic structure of the samples along with XRD. The FTIR (Fourier-transform infrared) spectroscopy was used to identify and analyze the molecular composition. The energy dispersive X-ray (EDX) spectroscopy was used to obtain qualitative chemical analysis, and utilized SEM pictures from the JEOL IT30rHR to study surface morphology. An UV–Vis absorption spectra (Lambda 650 PerkinElmer spectrophotometer) performed in the 200–900 nm wavelength range.

2.1. Photocatalytic performance

The methylene blue (MB) was used as an example of an industrial pollutant to assess the photocatalytic efficacy of both bare and Ho- and Yb-doped V_2O_5. The visible light source was a 300 W Xenon lamp, with a solar simulator added to screen UV radiation ($\lambda >$ 4200 Å). A 20-cm gap kept between the light source and the sample. Fig. 2 illustrates the apparatus setup for measuring photocatalytic activity. For each experiment, we mixed 200 mL of DI water with a 0.0001 mol of MB solution. On the other hand, an increase in photodegradation efficiency observed at 500 ppm concentration, this happens due to presence of RE doping. The solution agitated for half an hour in dark environment after adding the catalyst to create an adsorption-desorption symmetry between catalyst and dye. A 10 ml solution was taken from the original solution and centrifuged for 5 min at 5000 rpm to take absorbance spectra in intervel of 20 min.

2.2. Computational methodology

The Quantum ESPRESSO software's DFT framework was used to do the first-principle computations [44,45] based on experimentally obtained X-ray diffraction data at P = 0 GPa and room temperature (T = 300 K). The primitive orthorhombic phase (*Pmmn*) of V_2O_5 (VO) has been relaxed using the "variable-cell relaxation" approach inside the Broyden-Fletcher-Goldfarb-Shanno scheme [46–49]. The exchange-correlation term of the projector augmented wave (PAW) pseudopotential [50] was framed using the generalized gradient approximation (GGA) in conjunction with the Perdew-Burke-Ernzerhof for solids (PBEsol) functional [51]. The PAW pseudopotential has been taken into consideration for electron-ion interactions. The system's crystal structure is let to relax until the ambient circumstances cause total electronic energy and Hellmann-Feynman force to reach about $\sim 10^{-6}$ Ry and 10^{-3} a.u., respectively, as per the convergence criteria. Consideration has also been given to a Γ-centered $\boldsymbol{k}$-point $10 \times 10 \times 10$ grid for geometry optimization and self-consistent-field (SCF) computations.

To comprehend the electrical features of the co-doped VO system's tunability, a $3 \times 3 \times 2$ supercell comprising 252 atoms of bare

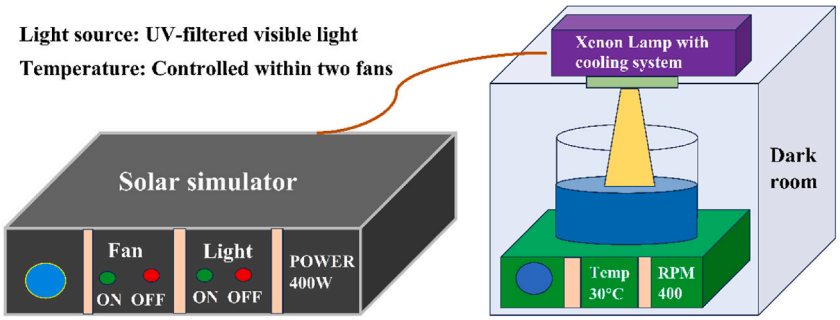

Fig. 2. Schematic diagram of experimental set up for measuring photocatalytic degradation under sun simulator.

VO crystal has been built. To create the 1.5 % Ho - 1.5 % Yb co-doped (HYVO) molecule, an equal number of Ho and Yb are then simultaneously doped by substituting the vanadium of the supercell. The valence electrons of atoms V, O, Ho, and Yb are classified as plane waves with a 60 Ry cut-off in kinetic energy. For non-SCF computations such as orbital-resolved projected atomic density of states (PDOS) and electronic band structures of the systems under study, a denser **k**-point grid of 20 × 20 × 20 has once again been taken into consideration. DFT calculations have included the on-site Coulomb repulsion + U_{dd} = 4.0 eV for the 3d atomic orbital of the V atom to accurately determine the electronic band gap (E_g) values of compounds [42,52].

3. Result and discussions

3.1. Structural properties

The XRD patterns of 3 % Ho (HVO), 3 % Yb (YVO), 1.5 % Ho and 1.5 % Yb (HYVO) co-doped V_2O_5 are shown in Fig. 3(a), along with V_2O_5 in its bare state. 3 % Ho and Yb doping into the V_2O_5 illustrates maximum photodegradation efficiency [42]. The XRD patterns match with the standard JCPDS #41–1426, indicating the formation of a stable orthorhombic structure [22]. The XRD patterns reveal no additional peaks, indicating the absence of secondary phases in the doping samples.

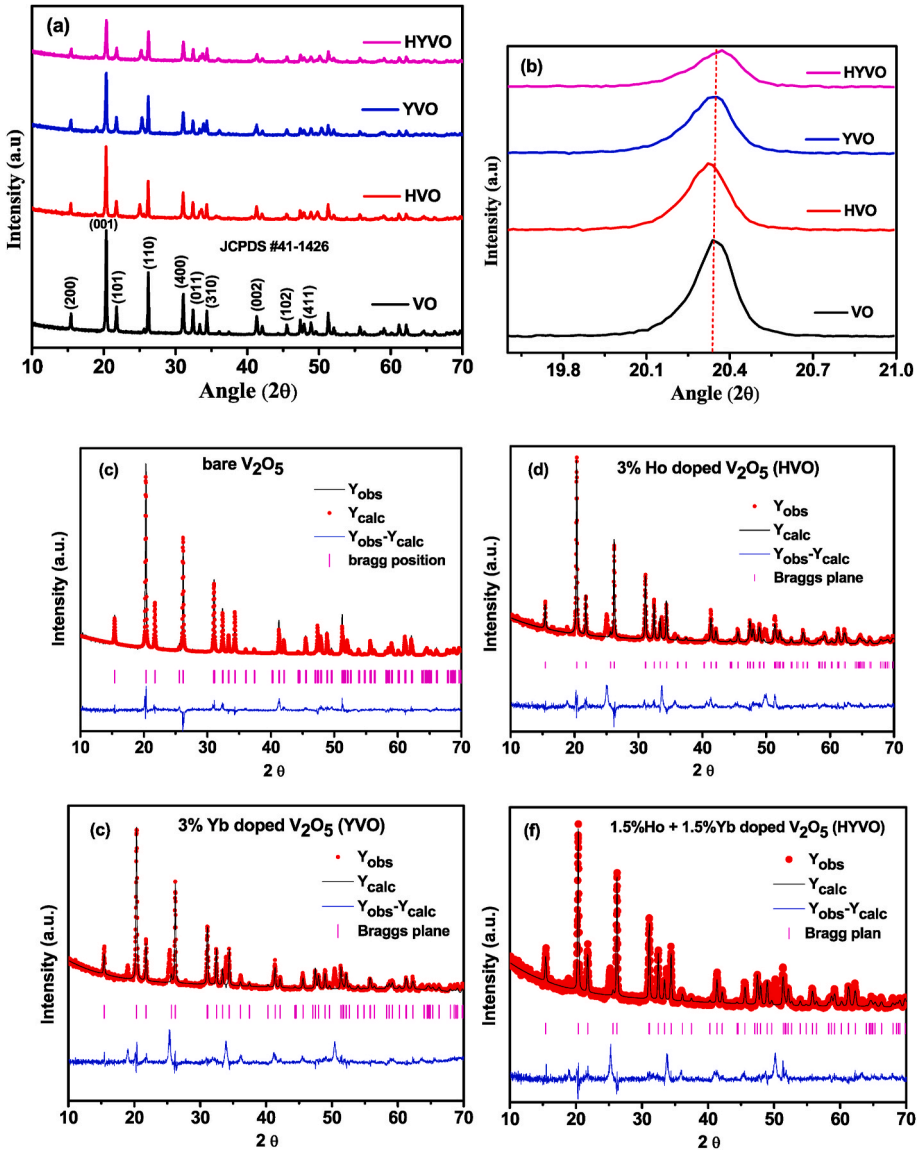

Fig. 3. (a) The XRD patterns (b) magnified pattern in the range of 19.6–21 degrees of all the doped and bare V_2O_5 samples. (c–f) Rietveld refinement of the bare V_2O_5, 3HVO (3 % Ho doped V_2O_5), 3YVO (3 % Yb doped V_2O_5) and HYVO (1.5%Ho - 1.5%Yb co-doped V_2O_5), respectively.

The peaks' strength diminishes as the doping concentration rises, suggesting that the samples' crystallinity is sacrificed in favor of a smaller crystallite size [23]. These differences in the crystal structure arise from the very large variation in ionic radius between V^{5+} (54 Å) and Ho^{3+} (89 Å) or Yb^{3+} (86 Å). The doped sample exhibits volume expansion compared to bared V_2O_5, as evidenced by the push of HVO and YVO peaks to lower 2θ values. However, peak shifts to higher 2θ values for HYVO demonstrating volume shrinkages in the doped sample as shown in Fig. 3(b).

Williamson-Hall (W-H) equation (1) is a simplified form of the Scherrer equation, which related the peak broadening (β) to the cryatallite size (D) and the internal lattice strain (ε). The equation is given by

$$\beta \cos\theta = \frac{K\lambda}{D} + 4\varepsilon \sin\theta \tag{1}$$

Where β = full width at half maxima (FWHM) of the peak, θ = Bragg angle, K = dimensionless constant called shape factor (value taken as 0.9). The W-H plot is shown in Fig. 4. The structural parameters of the samples can be calculated by plotting W-H equation and produces the following equations (2)–(4):

$$D = \frac{0.9\,\lambda}{\beta\, cos\,\theta} \tag{2}$$

$$\varepsilon = \frac{\beta}{4\, tan\,\theta} \tag{3}$$

$$\delta = \frac{1}{D^2} \tag{4}$$

The calculated parameters of the samples using equations (2)–(4) are illustrated in Table 1.

The VO crystallite size has been determined 71.1 nm and observes its rapid shrinkage as the elemental doping percentage increases. The data for HVO and YVO show the lowest values for crystallite size, suggesting a drop-in particle size with 3 % doping. Doping ions may explain this decrease in particle size by providing extra spaces for particle nucleation, transforming homogeneous nucleation into heterogeneous nucleation. The co-doped samples show an increase in D value, indicating that heterogeneous nucleation is slowing down and eventually giving way to homogenous nucleation, which in turn increases crystallite size [42,53]. But the dislocation density values and internal micro-strain are lower in the co-doped samples than in the doped samples. This means that the co-doped samples should have a faster and higher rate constant.

Rietveld refinement is a potent method for precisely deriving details about a material's crystal structure from diffraction data in X-ray or neutron diffraction. It is especially helpful in the analysis of complicated structures and those that alter as a result of doping or other modifications. The value of χ^2, a statistical metric used in Rietveld refinement to assess goodness of fit, is defined as follows: In the formula $\chi^2 = \sum \frac{(I_{obs} - I_{cal})}{\sigma^2}$, where I_{obs} = observed intensity, I_{cal} = calculated intensity, and σ = standard deviation of the observed intensity [54]. Figures (c–f) show the Rietveld refinement of the bare V_2O_5 and doped HVO, YVO and HYVO, respectively. The fitting parameters are tabulated in Table 1. Generally speaking, a smaller χ^2 value (around 1) denotes a better fit between the model and the observed data, indicating that the differences between the computed and observed values are compatible with the experimental uncertainties. However, if the model is capturing the important structural properties, a somewhat larger χ^2 value could be acceptable for more sophisticated models (to suit the doped samples) with numerous parameters. Since the model includes many phases for doped samples, a greater χ^2 (less than 5) may be appropriate if the data quality warrants it. For the examined samples, the χ^2 values are predicted to be about 3 (Table 1), although the fit quality suggests that the χ^2 values are appropriate and fall within an acceptable range.

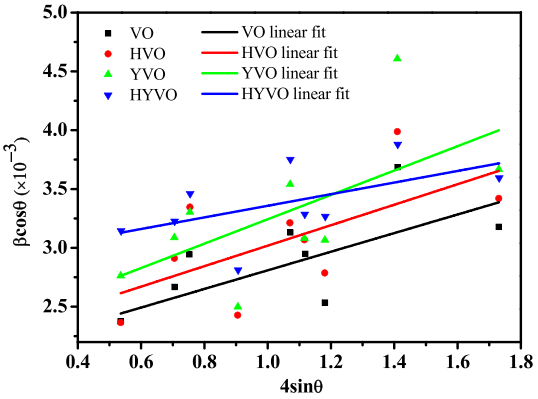

Fig. 4. The Williamson-Hall (W–H) plot.

Table 1
The various parameters of bare, doped and co-doped V_2O_5.

Sample	Crystallite size (nm)	Micro-Strain ($\times 10^{-3}$)	Dislocation density $\times 10^{-3}$ (nm^{-2})	Atomic coordinates	Fitting parameter (χ^2)
VO	71	2.76	1.98	V 0.14994 0.10484 0.18097 O 0.00000 1.02677 1.09702 O 0.14605 0.47935 1.21733 O 0.17956 0.00254 0.66374	3.28
HVO	36	5.43	7.56	V 0.15091 0.09928 0.19960 O 0.00000 1.02736 1.29933 O 0.14245 0.48610 1.13177 O 0.18138–0.00218 0.69161 Ho 0.15091 0.09928 0.19960	3.54
YVO	38	5.16	6.81	V 0.15480 0.09634 3.20175 O 0.00000 1.03080 4.24688 O 0.13384 0.46518 4.14760 O 0.17680–0.00198 3.72320 Yb 0.15480 0.09634 3.20175	3.84
HYVO	48	4.93	4.26	V 0.15348 0.10394 3.32205 O 0.00000 1.01460 4.35936 O 0.14028 0.47476 4.26121 O 0.17726–0.01172 3.81638 Ho 0.15348 0.10394 3.32205 Yb 0.15348 0.10394 3.32205	3.05

3.1.1. Morphplogical analysis

The SEM images have investigated the surface morphology of the synthesized HVO, YVO and HYVO along with the bare V_2O_5. Fig. 5(a and b) illustrates the various magnifications ($\times$ 25k and $\times$ 35k, respectively) of SEM images for the HYVO. Fig. 6 (upper panel) shows the SEM images for HVO, YVO, and VO. Co-doping into the VO significantly changes the particle morphology, as shown in Fig. 5 (a and b). Compared to their bare V_2O_5 and doped HVO and YVO, the particle size has significantly decreased. The pictures clearly show that doping elements create new nucleation compared to their original VO and encourage heterogeneous nucleation for the doped samples. This speeds up the process in the case of co-doping, which in turn lowers the chance of particles sticking together and eventually growing.

The EDX confirms the presence of desired elements like vanadium, oxygen, holmium and Ytterbium as shown in Fig. 5(c), which

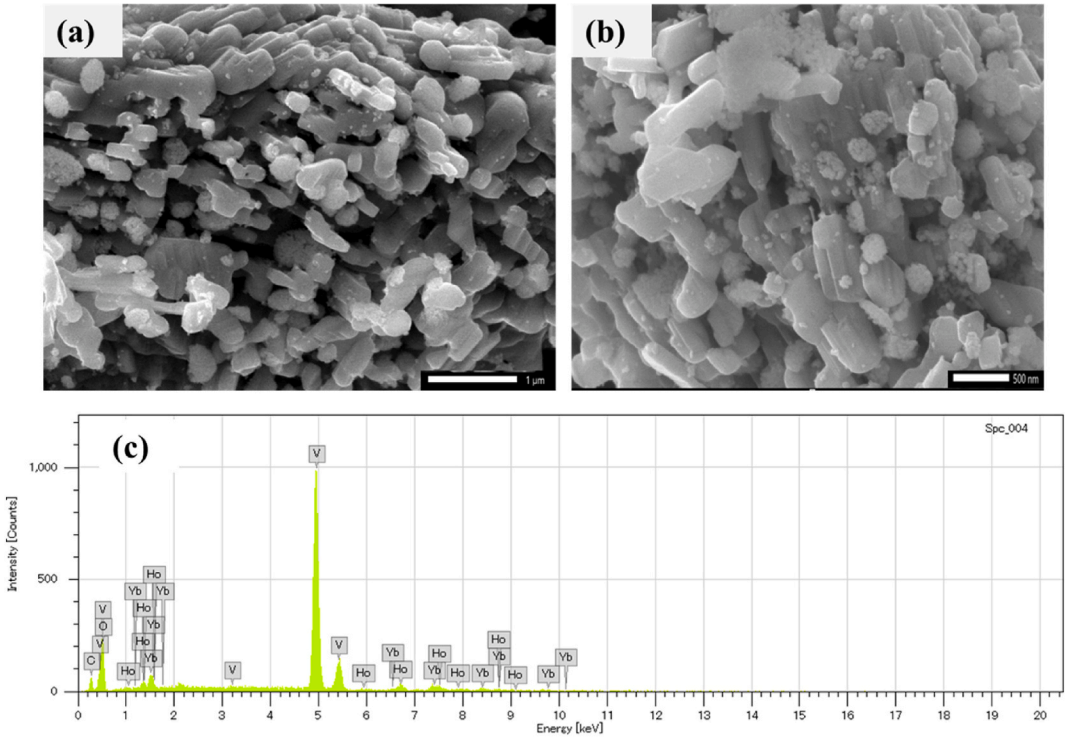

Fig. 5. (a,b) SEM images of co-doped HYVO with magnifications 25k and 35k, respectively. (c) EDX spectra of co-doped HYVO (1.5%Ho - 1.5%Yb doped into V_2O_5).

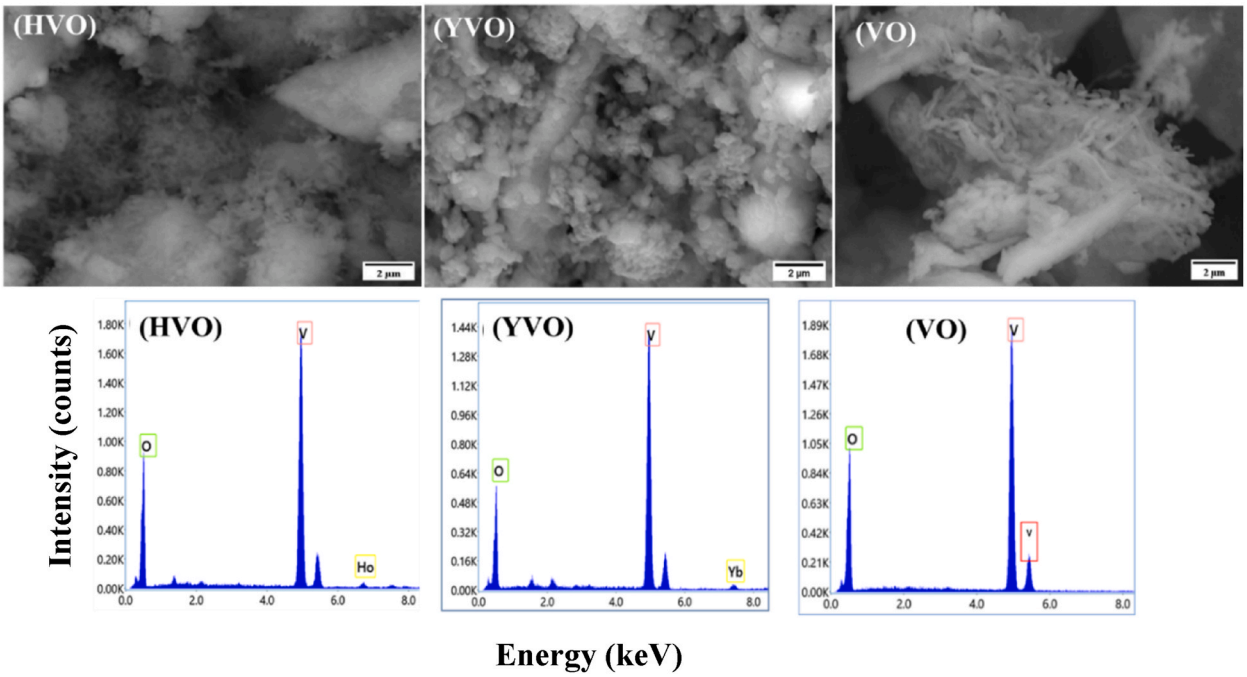

Fig. 6. (upper panel) SEM images of 3 % Ho (HVO), 3 % Yb (YVO) doped V_2O_5 and bare V_2O_5 (VO). (lower panel) EDX spectra of HVO, YVO and VO.

includes co-doped HYVO EDX spectra. Fig. 6 (lower panel) displays the bare EDX, revealing only V and O as additional peaks. Because of their high surface energy and irregular form, V_2O_5 particles tend to clump together. Gradually, as the doping increases, the agglomeration decreases and also becomes co-doped. The EDX spectra can be a great tool to check for the presence of predicted elements, even if they cannot be used to determine the precise percentage of elements in the entire sample. Apart from that, the elements' atomic percentage verified that V_2O_5 was successfully formed.

3.1.2. Functional group analysis by FTIR

By analyzing how compounds interact with infrared light, FTIR (Fourier Transform Infrared) analysis is used to identify and investigate substances. It basically measures the absorption of infrared light at various wavelengths by various chemical connections. FTIR spectra of the bare V_2O_5, HVO, YVO, and HYVO are recorded at room temperature and presented in Fig. 7. Between 400 and 1100 cm^{-1}, three primary, distinctive peaks of the samples are observed. The V-O-V vibration's (symmetric stretching, ν_s) modes have a peak at 412 cm^{-1}. The YVO has a greater V-O-V value of 420 cm^{-1}, while the HVO and HYVO have lower values of 414 and 416 cm^{-1} [43, 55–57]. This might have occurred because of the doping of RE ions Ho and Yb caused in the vanadium-oxygen bonds. For asymmetric stretching (ν_{as}) modes of V-O-V, rather large peaks emerge at 818 cm^{-1}. The bare V_2O_5 has a value of 828 cm^{-1}; this peak is moved to the lower values of 807, 821, and 817 cm^{-1} for the HVO, YVO, and HYVO, respectively. This is because of doping RE ions Ho and Yb

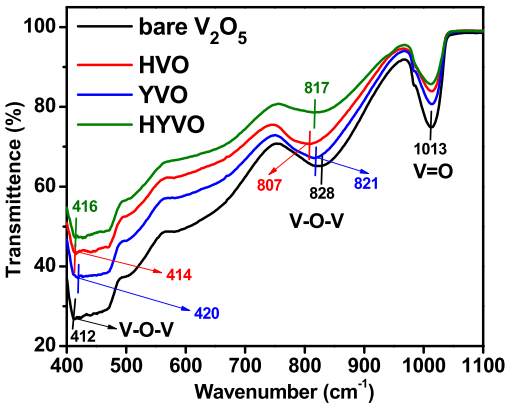

Fig. 7. The FTIR spectra of bare V_2O_5, HVO, YVO and HYVO measured at room temperature.

causes modifications in the V-O-V bonds. The terminal oxygen (V = O) vibrational bond is responsible for the third peak, which is seen at around 1013 cm^{-1}. At this point where peaks do not move considerably because of lower energy, doping ions could not impose strain on the vibrational bonds. Hence, together with XRD analysis, the FTIR spectra verified the materials' purity.

3.2. Optical features

The UV–visible absorption spectra of bare V_2O_5, HVO, YVO, and HYVO are shown in Fig. 8(a). The absorbance range at each wavelength is also shown. All samples in the visible range exhibit significant absorption due to the electron transition from O (2*p*) to V (3*d*) [40,53]. It is clear that the visible range's absorption is nearly constant up to 530 nm, after which the co-doped material exhibits reduced absorption. For the holmium/ytterbium doping, the empty orbitals of RE ions cause an increase in absorbance in the UV spectrum. The crystal structure becomes unbalanced in charge when Ho^{3+} or Yb^{3+} are replaced by V^{5+}, which is corrected by the formation of oxygen vacancies. These flaws also contribute to the improved absorbance of the doped V_2O_5 samples [22]. Another crucial parameter for describing the optical characteristics of the samples is the absorption edge (AE), which is the point in the absorption spectrum where a sharp discontinuity called the absorption discontinuity or absorption limit occurs. At that point, an ionization potential or an electronic transition are represented by the energy of an absorbed photon. Fig. 8(b) shows the computed AE of the samples. An increasing AE value from the bare indicates "red shift", while a lowering value indicates "blue shift" [42]. According to calculations, the blue shift edge for the VO, HVO, YVO, and HYVO samples is 585, 597, 625 and 627 nm, respectively. The co-doped HYVO sample exhibits superior catalytic performance compared to the other samples, as evidenced by its highest value compared to HVO and YVO.

Using the Tauc relationship in equation (5), the bandgap of the samples are determined.,

$$\alpha h\vartheta = A\left(h\vartheta - E_g\right)^n \tag{5}$$

Here, A = proportional constant, E_g = sample's bandgap, hν = photon energy, and α = absorption coefficient. Two alternative, n = 2 indicates direct bandgap whereas n = ½ specifies indirect bandgap that are used to classify the two different permitted transitions. Fig. 9 shows the samples' predicted bandgap as determined by the Tauc plot. The co-doped sample exhibits a larger bandgap compared to the doped and bare samples, suggesting potential enhancement in catalytic performance. It is suggested that when the co-doped material's defect content rises, radiative recombination is inhibited, which upturns the catalytic performance [58].

3.3. Photocatalytic measurements

The photocatalytic performance of the samples is measured using the MB characteristic peak in UV–visible absorption spectra, with a 500 ppm catalyst concentration [Fig. 10(a–c)]. The visible absorption spectra calculated at 611 and 660, 370 and 536, and 367 and 538 nm for the HVO, YVO, and HYVO, respectively, based on the two characteristic peaks in the absorption spectra. The degradation efficiency of dye determined by equation (6) because the decrease in intensity is proportional to the product's degradation.

$$\text{Dye removal efficiency} = \left(\frac{C_o - C_t}{C_o}\right) \times 100 \tag{6}$$

In this case, C_t indicates the equilibrium concentration at sampling time, while C_0 denotes the initial concentration. Our synthesized catalysts' kinetics may be measured using Langmuir Hinshelwood (L-H) kinetics in equation (7). [59], given below:

$$r = -\frac{dC}{dt} = \frac{k_T\, KC_t}{1 + KC_t} \tag{7}$$

K_r = time-dependent reaction rate, and K = adsorption equilibrium constant. Since relatively low concentration (1.0×10^{-4}

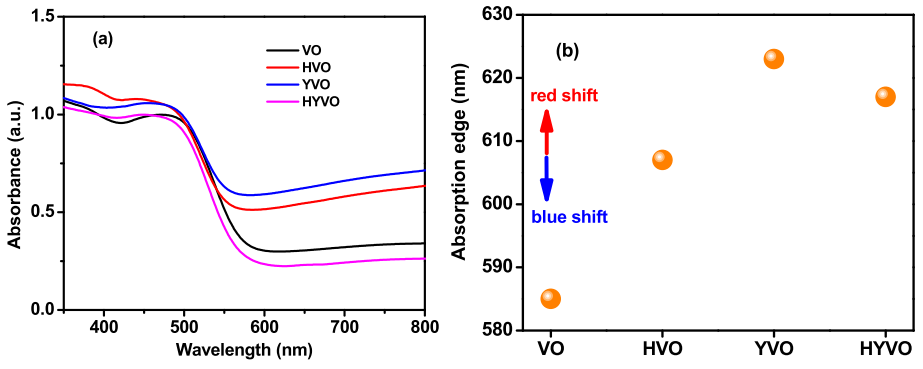

Fig. 8. (a) UV–visible absorption spectra for of bare VO, 3 % Ho (HVO), 3 % Yb (YVO) doped V_2O_5 and co-doped (HYVO). (b) the absorbance edge range of the samples.

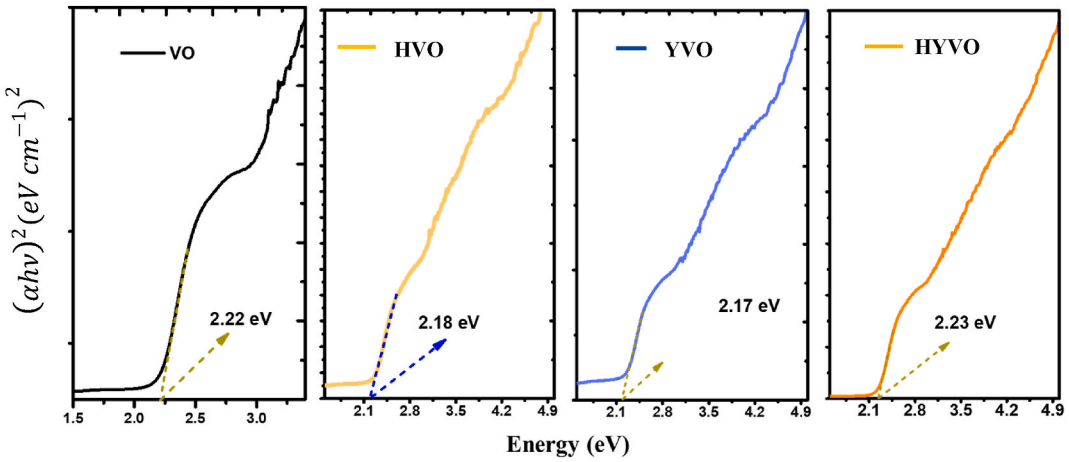

Fig. 9. Bandgap measurement of bare, doped and co-doped V_2O_5 sample by using Tauc formula.

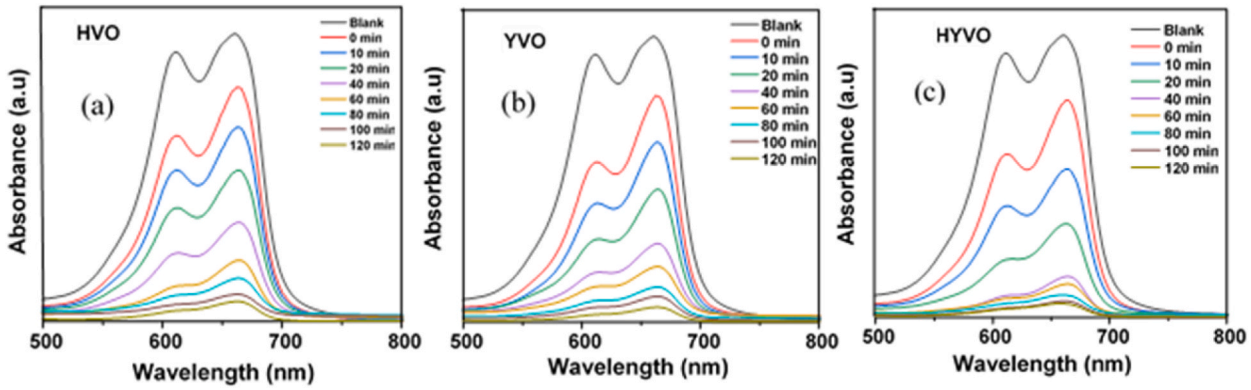

Fig. 10. Absorption spectra of MB degradation of doped HVO (a), YVO (b) and HYVO co-doped (c) of V_2O_5 [pH = 7, V_2O_5 = 500 ppm].

molarity) of MB was used, the first-order kinetic process may be roughly represented by equation (8) [60,61],

$$ln\left(\frac{C_0}{C_t}\right) = kt \tag{8}$$

Here, the pseudo-first-order rate constant is k. The slope of time dependent $ln\left(\frac{C_0}{C_t}\right)$ curve is used to compute this rate constant.

Fig. 11(a–c) displays time dependent degradation efficacies of HYVO, YVO, and HVO. Following 2 h of exposure to visible light, the samples exhibit increasing deterioration for co-doped HYVO and decreasing degradation for HVO. For HVO, YVO, and HYVO, the projected degradation percentages are 93, 94, and 95 %, respectively. A calculation of the rate constants is shown in Fig. 11(d) and values found to be 0.020, 0.022, and 0.024 min^{-1} for HVO, YVO, and HYVO, respectively. It's interesting to note that the rate constant of HYVO is over 2.5 times higher than that of the bare V_2O_5 sample [42]. As mention in the section on structural characteristics, the co-doped HYVO system showed a rate constant and degrading efficiency because of an increase in defects and bandgap, which in turn reduced radiative recombination. Based on the degradation and rate constant, co-doped sample HYVO may thus be a good option for photocatalysis.

Table 2 presents the results of our analysis, indicating that our HYVO degradation rate constant is the greatest of all the V_2O_5 particles presented. It is clear that the HYVO could be the finest option for photodegradation in V_2O_5. Rapid degradation is a must for a material to be recommended as the ideal catalyst.

Fig. 12 shows the likely pathways by which pollutants degrade. Equation shows how exposure to light energy equal to or higher than the band gap energy (E_g) promotes an excited electron in the photocatalyst's valence band (VB) to the conduction band (CB). A positive hole (h^+) is present in the VB while an electron (e^-) is produced in the CB by equation (9).

$$[1.5\%\ Ho/Yb.\ V_2O_5] + h\nu \rightarrow 1.5\%Ho/Yb.\ V_2O_5]\ (h^+{}_{VB} + e^-{}_{CB}) \tag{9}$$

Recombination occurs between the electron and hole or as a result of the surface charges. The recombination rate is finely regulated

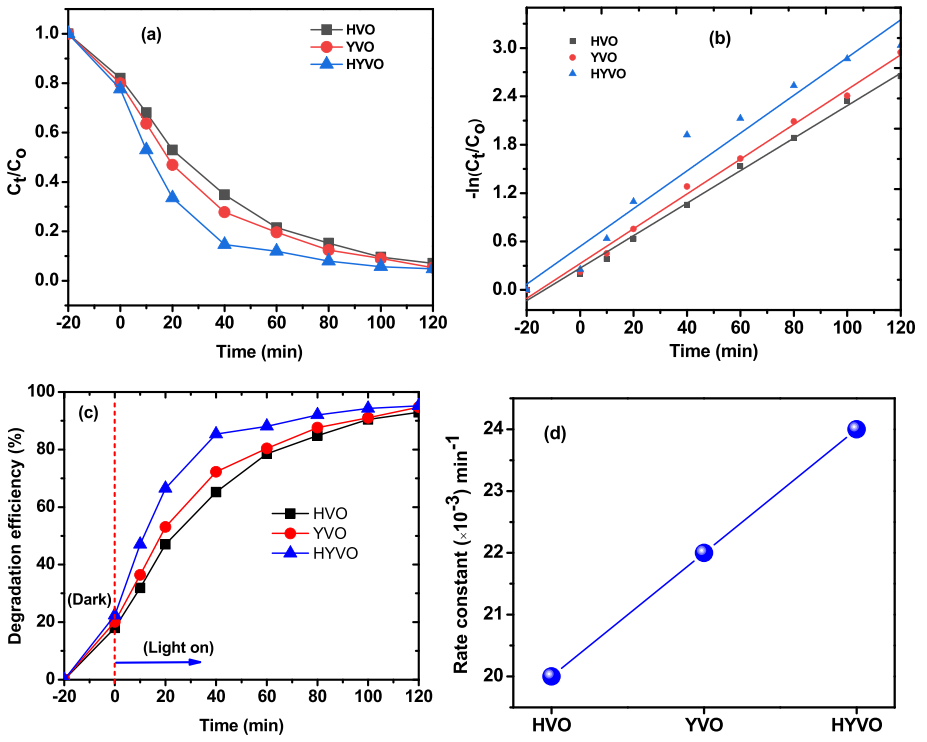

Fig. 11. Degradation of MB (a) and rate constant (b) as a function of time for HVO, YVO and HYVO. (c) degradation performance and (d) rate constant of degradation as a function of time of the samples.

Table 2
A summary of how different ions affect V_2O_5 in relation to MB photodegradation efficiency using visible light source.

Doping elements	V_2O_5 Concentration (ppm$\times 10^2$)	Dye Concentration (Molarity $\times 10^{-5}$)	Photodegradation performance (%)	Rate constant (min^{-1})	Ref
Gadolinium (5 wt%)	1	1.6	46	0.0055	[40]
Titanium (5 wt%)	2	1.0	82	0.014	[22]
Tin (3 mol.%)	2	–	95	0.0153	[62]
Cobalt (5 wt%)	5	0.1	91	0.02	[53]
Neodymium (7 mol.%)	10	1.6	99	0.014	[38]
Holmium (3 mol.%)	5	0.1	93	0.02	[42]
Ytterbium (3 mol.%)	5	0.1	95	0.022	[42]
Holmium (1.5 %) + Ytterbium (1.5 %)	5	0.1	95	0.024	This work

to determine the efficiency of photocatalysis. The pairs produced by photolysis, h^+_{VB} and e^-_{CB}, are transported to the surface of the catalyst. They dissolve oxygen and surface hydroxyl groups (OH) when they come into contact with water on the catalyst surface, creating extremely strong anions of superoxide and hydroxyl radicals. These electrons produced by photosynthesis possess the capacity to take up oxygen (O_2) and produce superoxide radicals ($\bullet O_2^-$), which in turn will catalyze other processes that try to lower the rate of recombination. On the other hand, when water (H_2O) and holes in the valence band mix, hydroxyl radicals can be produced that are represented in equations 10 and 11.

$$[1.5\%Ho/Yb.\ V_2O_5]\ (h^+_{VB}) + H_2O \text{ or } OH \rightarrow [1.5\%Ho/Yb.\ V_2O_5] + H^+ + {}^\bullet OH \quad (10)$$

$$[1.5\%Ho/Yb.\ V_2O_5]\ (e^-_{CB}) + O_2 \rightarrow [1.5\%Ho/Yb.\ V_2O_5] + {}^\bullet O_2^- \quad (11)$$

The dye is subsequently broken down into a number of chemical intermediates by attacking the potential radicals, and eventually it entirely mineralized into nitrate ions, carbon dioxide, water, and ammonium.

$$\text{CR dye} + OH + O_2{}^- \rightarrow \text{intermediates} \rightarrow CO_2\uparrow + H_2O$$

The potential of the valence band (E_{VB}) and conduction band (E_{CB}) can be determined for the V_2O_5 [63]:

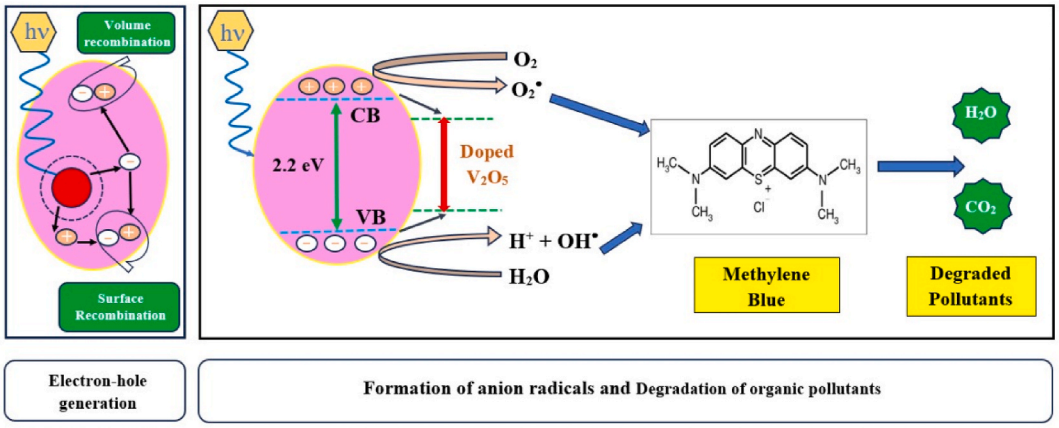

Fig. 12. Schematic illustration showing the effective pollutant degradation of rare-earth doped V_2O_5.

$$E_{VB} = \chi - E^e + 0.5\,E_g$$

$$E_{CB} = E_{VB} - E_g$$

In this case, χ denotes the V_2O_5's electronegativity (6.1 eV) [63]. E_g is V_2O_5's bandgap (2.22 eV), and E^e is energy of free electrons in the hydrogen scale (4.5 eV). The values of E_{CB} and E_{VB} are estimated 0.49 and 2.71 eV, respectively. It is acknowledged that doping components do not substantially alter the E_g, so that the E_{CB} and E_{VB} will essentially stay unchanged from the undoped sample. However, the doping elements produce a variety of defects by generating vanadium vacancies and interstitial oxygen, which adds to the bandgap's energy states. These energy states are thought to act as trapping spots to reduce recombination (e-h), increase photodegradation efficiency, prolong lifespan of the photo-excitons.

3.4. Gaining insight into the photocatalytic activity by first-principle DFT calculations

3.4.1. Crystal structures of bare and co-doped V_2O_5 systems

The VO system crystallizes to a primitive orthorhombic phase with space group no. 59 and *Pmmn* space group symmetry under ambient circumstances. Fig. 13(a) displays the optimal crystal structure of bare VO as determined by DFT calculation using GGA-PBEsol level of theory. The observed lattice parameters of the aforementioned compound are a = 3.575 Å, b = 4.665 Å, and c = 11.516 Å. These values exhibit good agreement with our previous research on the VO compound, as previously published [42].

To comprehend the superior catalytic performance of co-doped HYVO system (*vide supra*) from DFT calculation, two possible models of HYVO compound have been primarily considered by altering the positions of Ho and Yb atoms periodically inside the supercell geometry of VO system. Fig. 13 (b, c) displays the crystal structures of the models, that are designated as Type I and Type II in this context. The following mathematical equation [64–66] may be used to derive the corresponding defect formation energy per dopant (ΔE_{df}) in equation (12), which are used to determine the structural stabilities of Type I and Type II co-doped systems:

$$\Delta E_{df} = \frac{1}{N_{doped}}\left[E_{doped} - E_{bare} - N_{doped}\left(\mu_{doped} - \mu_V\right)\right] \tag{12}$$

where E_{doped} and E_{bare} represent total energies of co-doped and bare VO crystals respectively, N_{doped} is the number of total Ho and Yb dopants, μ_{doped} and μ_V denote the chemical potentials of Ho, Yb and V atoms respectively. The estimated ΔE_{df} values show that Type – I HYVO compound exhibits smaller ΔE_{df} (~−0.17 Ry) in contrast to its Type – II counterpart (ΔE_{df} ~ −0.14 Ry). The minimum ΔE_{df} (~−0.17 Ry) reflects that Type – I model of HYVO system is energetically most viable among other compounds under study.

3.4.2. Electronic properties of bare and co-doped V_2O_5 compounds

The electronic band structures (E-**k** diagrams) of the compounds under study have been calculated along the Γ→Y→T→Γ→X→U high-symmetry direction in order to comprehend the photocatalytic activities of Type I HYVO compounds and bare VO. The findings are shown in Fig. 14(A and B). The conduction band minimum (CBM) is found at high-symmetry point Γ in BZ, while the valence band maximum (VBM) of VO is located at T high-symmetry point [Fig. 14(A)]. The discovery indicates that bare VO has an indirect band gap semiconductor with an electron gap of approximately 2.22 eV. The compound's projected E_g value of 2.22 eV, derived from the PBEsol + U_{dd} calculations, agrees well with our experimental result obtained from our experimental absorption data (*vide supra*).

Interestingly, from Fig. 14 (B), alterations in the E-**k** diagram for HYVO system have been found. Although the CBM of co-doped system remains localized at the zone center Γ, the VBM however, is observed to move from high-symmetry point T to Γ. This result suggests that HYVO compound is a direct band gap semiconductor with E_g ~2.25 eV. The E_g value of the studied co-doped system, so estimated from PBEsol + U_{dd} level of theory, is also in close harmony with our experimental finding where the E_g value of HYVO is

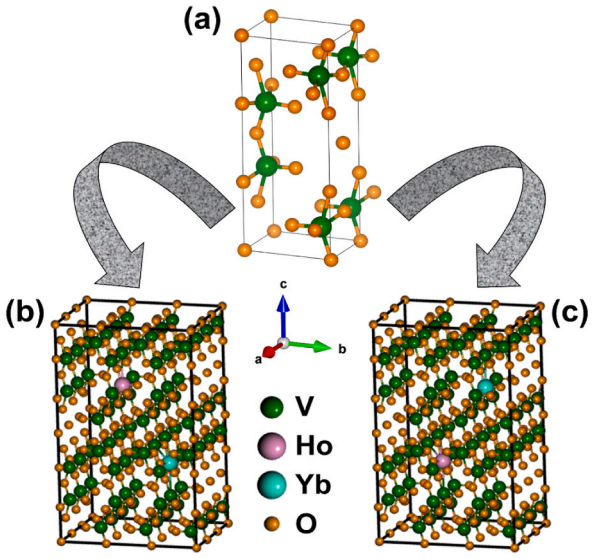

Fig. 13. (a) Optimized unit cell crystal structure of V_2O_5 system. Optimized supercell geometries for (b) Type – I and (c) Type – II HYVO compound as estimated from DFT calculations with GGA-PBEsol level of theory.

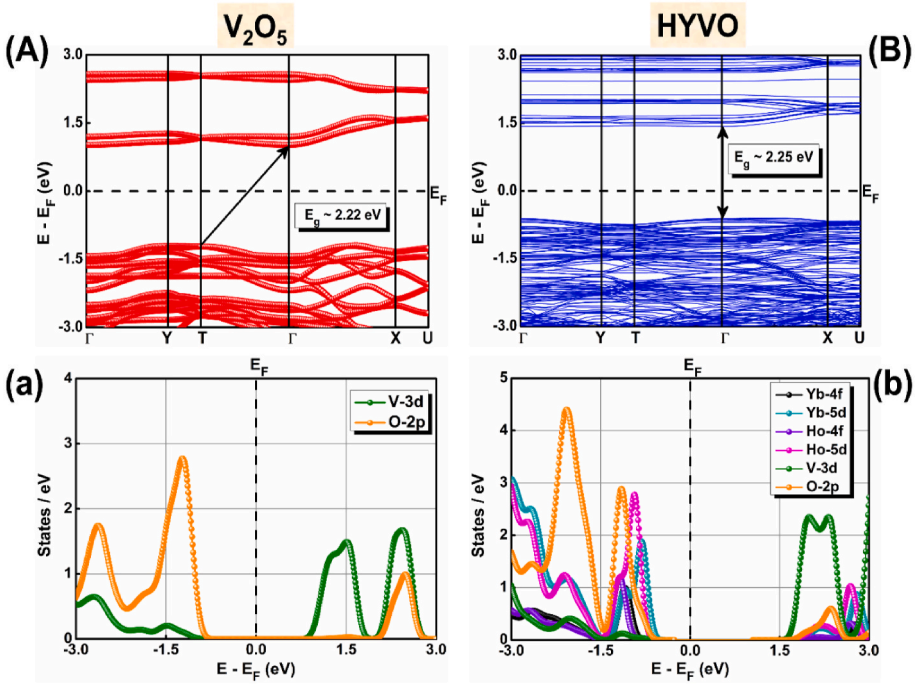

Fig. 14. Electronic band structures, orbital resolved PDOS of **(A, a)** bare and **(B, b)** 1.5 % Ho - 1.5 % Yb co-doped V_2O_5 systems as attained from PBEsol + U_{dd} level of theory. E_F denotes the Fermi energy level.

estimated to be ~2.23 eV (*vide supra*, cf. Fig. 2). While this estimated E_g (~2.25 eV), as observed in the DFT calculation, falls under the visible region (~551.04 nm) of electromagnetic wave spectrum, the direct band gap on the other hand may primarily signify the improved photocatalytic performance of co-doped system than the bare VO compound. In this regard, it is also relevant to mention that the presence of flat energy bands has been noticed in the E-**k** diagram of HYVO system [Fig. 14 (B)]. Flat energy bands suggest potential applications in nonlinear optics, photonics, photolysis, and energy storage devices due to smaller group velocity and larger effective charge carriers [42,67–69].

The orbital-resolved PDOS of the systems have been computed in order to properly comprehend the contributions of atomic orbitals in the photocatalytic performances of bare VO and HYVO complexes. The outcomes are displayed in Fig. 14(a and b). As can be

observed from Fig. 14(a), the bottom of the conduction bands, which range from 0 to +3 eV, mostly displays contributions from V-3d orbitals, whereas the top of the valence bands of bare VO, which range between −3 and 0 eV, originates predominantly from O-2p orbitals. Nonetheless, in the corresponding valence and conduction bands of VO close to the Fermi energy level (E_F), lesser contributions from the V-3d and O-2p orbitals have also been seen. There have also been seen distinct gap openings close to the E_F in each system's PDOS plot, resembling the E-**k** diagrams of bare and co-doped systems. Remarkably, notable modifications have been noted in the PDOS spectra of the HYVO molecule, as illustrated in Fig. 14(b). O-2p orbitals and the 5d orbitals of the Ho and Yb atoms have been seen to make up the majority of the contributions in the valence bands close to E_F in Fig. 14(b). Nonetheless, it is discovered that the relative weight of Ho's 5d orbitals is greater than that of Yb-5d orbitals. Furthermore, the top of the valence bands of the HYVO system has also shown minor contributions from the 4f orbitals of the Ho and Yb atoms. Collectively, these facts suggest that the RE elements holmium and Ytterbium would be important in improving the co-doped compound's photocatalytic capabilities, which is consistent with our experimental results (*vide supra*).

4. Conclusions

The co-doped V_2O_5 has been formed using a facile mild hydrothermal method that is friendly to the environment, containing 1.5 % (Ho) and 1.5 % (Yb). The research looked at how the doping elements affect the photocatalytic activity of co-doped V_2O_5, comparing it to both bare V_2O_5 and V_2O_5 that had been doped with 3 % Ho and 3 % Yb. The co-doping enhances the production of oxygen vacancies and suppresses radiative recombination, leading to a rise in absorbance. The lower dislocation density (4.26×10^{-3} nm^{-2}) and internal micro-strain (4.93×10^{-3}) of the RE elements make it easier to fix the charge imbalance, which improves absorption and gives the best degradation efficiency (95 % vs. 94 % for Ho-doped V_2O_5 and Yb-doped V_2O_5). Experimental research established the bandgap of co-doped samples at 2.23 eV, in agreement with DFT (2.25 eV), which reduces radiative recombination and increases degrading efficiency compared to doped samples. Notably, the doping samples exhibit the greatest rate constant (4.93×10^{-3} min^{-1}), indicating a faster deterioration process than the doped system. The co-doped V_2O_5, with a 95 % degradation efficiency and a rate constant, indicates that there is a synergistic effect that promotes a rapid degradation process in the system. Therefore, 1.5 % HVO and 1.5 % YVO co-doped V_2O_5 can be recommended as an extremely effective and quick catalyst to address major environmental pollution problems.

Funding statement

No funding was used for this study.

Data availability

Data will be made available on request.

CRediT authorship contribution statement

M.M. Uddin: Writing – review & editing, Writing – original draft, Supervision, Methodology, Investigation, Formal analysis, Data curation, Conceptualization. **M.Z. Hossain:** Writing – review & editing, Writing – original draft, Investigation. **M.H. Kabir:** Writing – review & editing, Writing – original draft, Investigation, Data curation. **S. Ghosh:** Writing – review & editing, Writing – original draft, Formal analysis. **M.H. Haque:** Investigation, Formal analysis. **M.M. Hossain:** Writing – review & editing, Writing – original draft. **M. A. Ali:** Writing – review & editing, Writing – original draft. **Md Akhtaruzzaman:** Writing – review & editing, Writing – original draft, Formal analysis. **Abdulaziz M. Alanazi:** Writing – review & editing, Writing – original draft. **S. Mondal:** Writing – review & editing, Writing – original draft, Data curation. **J. Chowdhury:** Writing – review & editing, Writing – original draft. **D. Karmakar:** Writing – review & editing, Writing – original draft, Formal analysis. **D. Jana:** Writing – review & editing, Writing – original draft.

Declaration of competing interest

The authors declare the following financial interests/personal relationships which may be considered as potential competing interests:Prof. Dr. Md Mohi Uddin reports writing assistance was provided by Department of Physics, University of Calcutta, West Bengal, India. If there are other authors, they declare that they have no known competing financial interests or personal relationships that could have appeared to influence the work reported in this paper.

Acknowledgments

The authors are acknowledged UGC, Bangladesh grant number (37, 0000.073.07.101.23.2838), 'PARAM Kamrupa' at IIT Guwahati that is executed by C-DAC and maintained by the Ministry of Electronics and Information Technology (MeitY) and DST, Government of India. S. Ghosh is also acknowledged UGC, India for providing the UGC-NET (JRF). The researchers also gratitude to the Deanship of Graduate Studies and Scientific Research at the Islamic University of Madinah for the support provided to the Post-Publishing Program.

References

[1] R. Vinu, Giridhar Madras, Environmental remediation by photocatalysis, J. Indian Inst. Sci. 90 (2) (2010) 189–230.
[2] M. Mishra, D.-M. Chun, α-Fe 2 O 3 as a photocatalytic material: a review, Appl. Catal. Gen. 498 (2015) 126–141, https://doi.org/10.1016/j.apcata.2015.03.023.
[3] Y. Lu, H. Zhang, D. Fan, Z. Chen, X. Yang, Coupling solar-driven photothermal effect into photocatalysis for sustainable water treatment, J. Hazard Mater. 423 (2022) 127128, https://doi.org/10.1016/j.jhazmat.2021.127128.
[4] R. Abazari, S. Sanati, L.A. Saghatforoush, Non-aggregated divanadium pentoxide nanoparticles: a one-step facile synthesis. Morphological, structural, compositional, optical properties and photocatalytic activities, Chem. Eng. J. 236 (2014) 82–90, https://doi.org/10.1016/j.cej.2013.09.056.
[5] M.M. Khan, S.F. Adil, A. Al-Mayouf, Metal oxides as photocatalysts, J. Saudi Chem. Soc. 19 (2015) 462–464, https://doi.org/10.1016/j.jscs.2015.04.003.
[6] A.B. Djurišić, Y.H. Leung, A.M.C. Ng, Strategies for improving the efficiency of semiconductor metal oxide photocatalysis, Mater. Horiz. 1 (2014) 400–410, https://doi.org/10.1039/C4MH00031E.
[7] H. Wang, L. Zhang, Z. Chen, J. Hu, S. Li, Z. Wang, J. Liu, X. Wang, Semiconductor heterojunction photocatalysts: design, construction, and photocatalytic performances, Chem. Soc. Rev. 43 (2014) 5234–5244, https://doi.org/10.1039/C4CS00126E.
[8] M. Serda, F.G. Becker, M. Cleary, R.M. Team, H. Holtermann, D. The, N. Agenda, P. Science, S.K. Sk, R. Hinnebusch, R.H. A, I. Rabinovich, Y. Olmert, D.Q.G.L. Q. Uld, W.K.H.U. Ri, V. Lq, W.K.H. Frxqwu, E. Zklfk, L. V Edvhg, R.Q. Wkh, F.G. Becker, N. Aboueldahab, R. Khalaf, L.R. De Elvira, T. Zintl, R. Hinnebusch, M. Karimi, S.M.M. Shafaee, D.O. driscoll, S. Watts, J. Kavanagh, B. Frederick, T. Norlen, A. O'Mahony, P. Voorhies, T. Szayna, N. Spalding, M.O. Jackson, M. Morelli, B. Satpathy, B. Muniapan, M. Dass, P. Katsamunska, Y. Pamuk, A. Stahn, E. Commission, T.E.D. Piccone, M.K. Annan, S. Djankov, M. ReynalQuerol, M. Couttenier, R. Soubeyran, P. Vym, E. Prague, W. Bank, C. Bodea, N. Sambanis, A. Florea, A. Florea, M. Karimi, S.M.M. Shafaee, N. Spalding, N. Sambanis, ج. فاطمی, Synteza i aktywność biologiczna nowych analogów tiosemikarbazonowych chelatorów żelaza, Uniwersytet Śląski 7 (2013) 343–354.
[9] E. Pelizzetti, C. Minero, Metal oxides as photocatalysts for environmental detoxification, Comments Mod. Chem. 15 (1994) 297–337, https://doi.org/10.1080/02603599408035846.
[10] B. Yan, L. Liao, Y. You, X. Xu, Z. Zheng, Z. Shen, J. Ma, L. Jong, T. Yu, Single-crystalline v2O5 ultralong nanoribbon waveguides, Adv. Mater. 21 (2009) 2436–2440, https://doi.org/10.1002/adma.200803684.
[11] C.C. Wang, C.L. Lu, F.S. Shieu, H.C. Shih, Structure and photoluminescence properties of thermally synthesized V2O5 and al-doped V2O5 nanostructures, Materials 14 (2021), https://doi.org/10.3390/ma14020359.
[12] W. Avansi, V.R. de Mendonça, O.F. Lopes, C. Ribeiro, Vanadium pentoxide 1-D nanostructures applied to dye removal from aqueous systems by coupling adsorption and visible-light photodegradation, RSC Adv. 5 (2015) 12000–12006, https://doi.org/10.1039/C4RA12788A.
[13] B. Liu, D. Yin, F. Zhao, K.K. Khaing, T. Chen, C. Wu, L. Deng, L. Li, K. Huang, Y. Zhang, Construction of a novel Z-scheme heterojunction with molecular grafted carbon nitride nanosheets and V $_2$ O $_5$ for highly efficient photocatalysis, J. Phys. Chem. C 123 (2019) 4193–4203, https://doi.org/10.1021/acs.jpcc.8b11361.
[14] H. Liu, Y. Gao, J. Zhou, X. Liu, Z. Chen, C. Cao, H. Luo, M. Kanehira, Growth of oriented vanadium pentaoxide nanostructures on transparent conducting substrates and their applications in photocatalysis, J. Solid State Chem. 214 (2014) 79–85, https://doi.org/10.1016/j.jssc.2013.10.020.
[15] H.-L. Fei, H.-J. Zhou, J.-G. Wang, P.-C. Sun, D.-T. Ding, T.-H. Chen, Synthesis of hollow V2O5 microspheres and application to photocatalysis, Solid State Sci. 10 (2008) 1276–1284, https://doi.org/10.1016/j.solidstatesciences.2007.12.026.
[16] M.M. Sajid, N.A. Shad, Y. Javed, S.B. Khan, Z. Zhang, N. Amin, H. Zhai, Preparation and characterization of Vanadium pentoxide (V2O5) for photocatalytic degradation of monoazo and diazo dyes, Surface. Interfac. 19 (2020) 100502, https://doi.org/10.1016/j.surfin.2020.100502.
[17] D. Vernardou, E. Spanakis, G. Kenanakis, E. Koudoumas, N. Katsarakis, Hydrothermal growth of V2O5 photoactive films at low temperatures, Mater. Chem. Phys. 124 (2010) 319–322, https://doi.org/10.1016/j.matchemphys.2010.06.040.
[18] M. Aslam, I.M.I. Ismail, N. Salah, S. Chandrasekaran, M.T. Qamar, A. Hameed, Evaluation of sunlight induced structural changes and their effect on the photocatalytic activity of V2O5 for the degradation of phenols, J. Hazard Mater. 286 (2015) 127–135, https://doi.org/10.1016/j.jhazmat.2014.12.022.
[19] M. Shanmugam, A. Alsalme, A. Alghamdi, R. Jayavel, Enhanced photocatalytic performance of the graphene-V2O5 nanocomposite in the degradation of methylene blue dye under direct sunlight, ACS Appl. Mater. Interfaces 7 (2015) 14905–14911, https://doi.org/10.1021/acsami.5b02715.
[20] N. Asim, S. Radiman, M.A. Yarmo, M.S. Banaye Golriz, Vanadium pentoxide: synthesis and characterization of nanorod and nanoparticle V2O5 using CTAB micelle solution, Microporous Mesoporous Mater. 120 (2009) 397–401, https://doi.org/10.1016/j.micromeso.2008.12.013.
[21] C.V. Reddy, R.R. Kakarla, B. Cheolho, J. Shim, M. Rezakazemi, T.M. Aminabhavi, Highly efficient photodegradation of toxic organic pollutants using Cu-doped V2O5 nanosheets under visible light, Chemosphere 311 (2023) 137015, https://doi.org/10.1016/j.chemosphere.2022.137015.
[22] M. Neelima, S. Vandana, A. Kathirvel, M. Sivakumar, A.U. Maheswari, Titanium doped V2O5 nanostructures by chemical synthesis for photocatalytic performance enhancement, Optik 252 (2022), https://doi.org/10.1016/j.ijleo.2021.168516.
[23] N. Bashir, S. Zulfiqar, S. Munir, M.M. Ibrahim, M.F.A. Taleb, S.M. El-Bahy, M. Suleman, M. Shahid, Sodium doped-V2O5 nanorods for visible light irradiated photocatalytic performance for the degradation of Rh-dye, Ceram. Int. 48 (2022), https://doi.org/10.1016/j.ceramint.2021.12.312.
[24] M. Panagopoulou, D. Vernardou, E. Koudoumas, N. Katsarakis, D. Tsoukalas, Y.S. Raptis, Tunable properties of Mg-doped V2O5 thin films for energy applications: Li-ion batteries and electrochromics, J. Phys. Chem. C 121 (2017), https://doi.org/10.1021/acs.jpcc.6b09018.
[25] Y.X. Wei, Y.B. Ma, M. Chen, W.M. Liu, L. Li, Y. Yan, Electrochemical investigation of electrochromic device based on WO3 and Ti doped V2O5 films by using electrolyte containing ferrocene, J. Electroanal. Chem. 807 (2017), https://doi.org/10.1016/j.jelechem.2017.11.007.
[26] C. Peng, F. Xiao, J. Yang, Z. Li, G. Lei, Q. Xiao, Y. Ding, Z. Hu, Carbon-encapsulated Mn-doped V2O5 nanorods with long span life for high-power rechargeable lithium batteries, Electrochim. Acta 192 (2016), https://doi.org/10.1016/j.electacta.2016.01.195.
[27] I. Pradeep, E.R. Kumar, N. Suriyanaranan, C. Srinivas, N.V. Rao, Structural, optical and electrical properties of pure and Fe doped V2O5 nanoparticles for junction diode fabrications, J. Mater. Sci. Mater. Electron. 29 (2018), https://doi.org/10.1007/s10854-018-9024-1.
[28] P.S. Menon, S.A. Thomas, M.P. Anjana, C. Beryl, D. Sajan, G. Vinitha, R. Philip, The role of defects in the nonlinear optical absorption behavior of bare and Co-doped V2O5 layered 2D nanostructures, J. Alloys Compd. 907 (2022), https://doi.org/10.1016/j.jallcom.2022.164413.
[29] M. Rafique, M. Hamza, M.B. Tahir, S. Muhammad, A.G. Al-Sehemi, Facile hydrothermal synthesis of highly efficient and visible light-driven Ni-doped V2O5 photocatalyst for degradation of Rhodamine B dye, J. Mater. Sci. Mater. Electron. 31 (2020), https://doi.org/10.1007/s10854-020-03844-3.
[30] Y. Liu, W. Guo, H. Guo, X. Ren, Q. Xu, Cu (II)-doped V2O5 mediated persulfate activation for heterogeneous catalytic degradation of benzotriazole in aqueous solution, Separation and Purification Technology 230 (2020), https://doi.org/10.1016/j.seppur.2019.115848.
[31] N.S. Kumar, J.H. Chang, M.S. Ho, B. Balraj, S. Chandrasekar, B. Mohanbabu, M. Gowtham, D. Guo, K. Mohanraj, Impact of Zn2+ doping on the structural, morphological and photodiode properties of V2O5 nanorods, J. Inorg. Organomet. Polym. Mater. 31 (2021), https://doi.org/10.1007/s10904-020-01751-y.
[32] A. Saliman, Synthesis and characterization of Zr-doped vanadium oxide nanotubes, Am. J. Chem. Eng. 6 (2018), https://doi.org/10.11648/j.ajche.20180604.12.
[33] S. Rajeshwari, J.S. Kumar, R.T. Rajendrakumar, N. Ponpandian, P. Thangadurai, Influence of Sn ion doping on the photocatalytic performance of V2O5 nanorods prepared by hydrothermal method, Mater. Res. Express 5 (2018), https://doi.org/10.1088/2053-1591/aaab0a.
[34] C. Yan, L. Liu, Sn-doped V2O5 nanoparticles as catalyst for fast removal of ammonia in air via PEC and PEC-MFC, Chem. Eng. J. 392 (2020), https://doi.org/10.1016/j.cej.2019.123738.
[35] J.H. Yao, Z.L. Yin, Z.G. Zou, Y.W. Li, Y-doped V2O5 with enhanced lithium storage performance, RSC Adv. 7 (2017), https://doi.org/10.1039/c7ra03885b.
[36] M.A. Centeno, P. Malet, I. Carrizosa, J.A. Odriozola, Lanthanide doped V2O5/Al2O3 catalysts: structure - activity relationship in the SCR of NOx, J. Phys. Chem. B 104 (2000), https://doi.org/10.1021/jp993084a.
[37] B. Etemadi, J. Mazloom, F.E. Ghodsi, Phase transition and surface morphology effects on optical, electrical and lithiation/delithiation behavior of nanostructured Ce-doped V2O5 thin films, Mater. Sci. Semicond. Process. 61 (2017) 99–106, https://doi.org/10.1016/J.MSSP.2016.12.035.
[38] G.R. Navyashree, K. Hareesh, D. V Sunitha, H. Nagabhushana, G. Nagaraju, Photocatalytic degradation performance of Nd3+ doped V2O5 nanostructures, Mater. Res. Express 5 (2018), https://doi.org/10.1088/2053-1591/aad373.

[39] C.C. Wang, C.L. Lu, F.S. Shieu, H.C. Shih, Enhanced photoluminescence properties of Ga-doped V2O5 nanorods via defect structures, Chem. Phys. Lett. 738 (2020), https://doi.org/10.1016/j.cplett.2019.136864.
[40] H. Chaudhary, K. Chaudhary, S. Zulfiqar, M.S. Saif, I.A. Alsafari, I. Shakir, P.O. Agboola, M. Safdar, M.F. Warsi, Fabrication of reduced Graphene Oxide supported Gd3+ doped V2O5 nanorod arrays for superior photocatalytic and antibacterial activities, Ceram. Int. 47 (2021), https://doi.org/10.1016/j.ceramint.2021.08.146.
[41] A. Mehtab, J. Ahmed, S.M. Alshehri, Y. Mao, T. Ahmad, Rare earth doped metal oxide nanoparticles for photocatalysis: a perspective, Nanotechnology 33 (2022), https://doi.org/10.1088/1361-6528/ac43e7.
[42] M.H. Kabir, M.Z. Hossain, M.A. Jalil, S. Ghosh, M.M. Hossain, M.A. Ali, M.U. Khandaker, D. Jana, M.M. Rahman, M.K. Hossain, J. Chowdhury, M. Kazi, M. M. Uddin, The efficacy of rare-earth doped V2O5 photocatalyst for removal of pollutants from industrial wastewater, Opt. Mater. 147 (2024) 114724, https://doi.org/10.1016/j.optmat.2023.114724.
[43] M.A. Jalil, M.N.I. Khan, S.K. Mandal, F.-U.-Z. Chowdhury, M.M. Hossain, D. Jana, M.S. Alam, M.M. Uddin, Impact of reaction temperatures on the particle size of V2O5 synthesized by facile hydrothermal technique and photocatalytic efficacy in dye degradation, AIP Adv. 13 (2023) 15010, https://doi.org/10.1063/5.0125200.
[44] P. Giannozzi, O. Baseggio, P. Bonfà, D. Brunato, R. Car, I. Carnimeo, C. Cavazzoni, S. de Gironcoli, P. Delugas, F.F. Ruffino, A. Ferretti, N. Marzari, I. Timrov, A. Urru, S. Baroni, Quantum ESPRESSO toward the exascale, J. Chem. Phys. 152 (2020) 154105, https://doi.org/10.1063/5.0005082.
[45] P. Giannozzi, O. Andreussi, T. Brumme, O. Bunau, M.B. Nardelli, M. Calandra, R. Car, C. Cavazzoni, D. Ceresoli, M. Cococcioni, N. Colonna, I. Carnimeo, A. D. Corso, S. de Gironcoli, P. Delugas, R.A. DiStasio, A. Ferretti, A. Floris, G. Fratesi, G. Fugallo, R. Gebauer, U. Gerstmann, F. Giustino, T. Gorni, J. Jia, M. Kawamura, H.-Y. Ko, A. Kokalj, E. Küçükbenli, M. Lazzeri, M. Marsili, N. Marzari, F. Mauri, N.L. Nguyen, H.-V. Nguyen, A. Otero-de-la-Roza, L. Paulatto, S. Poncé, D. Rocca, R. Sabatini, B. Santra, M. Schlipf, A.P. Seitsonen, A. Smogunov, I. Timrov, T. Thonhauser, P. Umari, N. Vast, X. Wu, S. Baroni, Advanced capabilities for materials modelling with Quantum ESPRESSO, J. Phys. Condens. Matter 29 (2017) 465901, https://doi.org/10.1088/1361-648X/aa8f79.
[46] C.G. Broyden, The convergence of a class of double-rank minimization algorithms 1. General considerations, IMA J, Appl. Math. 6 (1970) 76–90, https://doi.org/10.1093/imamat/6.1.76.
[47] R. Fletcher, A new approach to variable metric algorithms, Comput. J. 13 (1970) 317–322, https://doi.org/10.1093/comjnl/13.3.317.
[48] D. Goldfarb, A family of variable-metric methods derived by variational means, Math. Comp. 24 (1970) 23–26, https://doi.org/10.2307/2004873.
[49] D.F. Shanno, Conditioning of quasi-Newton methods for function minimization, Math. Comp. 24 (1970) 647–656, https://doi.org/10.2307/2004840.
[50] A.D. Corso, Pseudopotentials periodic table: from H to Pu, Comput. Mater. Sci. 95 (2014) 337–350, https://doi.org/10.1016/j.commatsci.2014.07.043.
[51] J.P. Perdew, A. Ruzsinszky, G.I. Csonka, O.A. Vydrov, G.E. Scuseria, L.A. Constantin, X. Zhou, K. Burke, Restoring the density-gradient expansion for exchange in solids and surfaces, Phys. Rev. Lett. 100 (2008) 136406, https://doi.org/10.1103/PhysRevLett.100.136406.
[52] D.O. Scanlon, A. Walsh, B.J. Morgan, G.W. Watson, An ab initio study of reduction of V2O5 through the formation of oxygen vacancies and Li intercalation, J. Phys. Chem. C 112 (2008) 9903–9911, https://doi.org/10.1021/jp711334f.
[53] R. Suresh, K. Giribabu, R. Manigandan, S. Munusamy, S.P. Kumar, S. Muthamizh, A. Stephen, V. Narayanan, Doping of Co into V2O5 nanoparticles enhances photodegradation of methylene blue, J. Alloys Compd. 598 (2014), https://doi.org/10.1016/j.jallcom.2014.02.041.
[54] B.H. Toby, R factors in Rietveld analysis: how good is good enough? Powder Diffr. 21 (2006) 67–70, https://doi.org/10.1154/1.2179804.
[55] A. Kumar, P.P. Sahay, Influence of Ti doping on the microstructural and electrochromic properties of dip-coated nanocrystalline V2O5 thin films, J. Sol. Gel Sci. Technol. 95 (2020) 34–51, https://doi.org/10.1007/s10971-020-05298-9.
[56] S. Mukhtar, M. Liu, J. Han, W. Gao, Removal of rhodamine B from aqueous solutions using vanadium pentoxide/titanium butyl oxide hybrid xerogels, Chin. Phys. B 26 (2017), https://doi.org/10.1088/1674-1056/26/5/058202.
[57] W.C., V. Subba Reddy, Wei Jin, Quan-Yao Zhu, Polymer intercalated V2O5 nanostructured cathodes for secondary batteries, Eur. Phys. J. Appl. Phys. 184 (2006) 177–184, https://doi.org/10.1051/epjap.
[58] M.H. Kabir, H. Ibrahim, S.A. Ayon, M.M. Billah, S. Neaz, Structural, nonlinear optical and antimicrobial properties of sol-gel derived, Fe-doped CuO thin films, Heliyon 8 (2022) e10609, https://doi.org/10.1016/j.heliyon.2022.e10609.
[59] K.V. Kumar, K. Porkodi, F. Rocha, Langmuir-Hinshelwood kinetics - a theoretical study, Catal. Commun. 9 (2008), https://doi.org/10.1016/j.catcom.2007.05.019.
[60] I.K. Konstantinou, T.A. Albanis, Photocatalytic transformation of pesticides in aqueous titanium dioxide suspensions using artificial and solar light: intermediates and degradation pathways, Applied Catalysis B: Environmental. 42 (2003), https://doi.org/10.1016/S0926-3373(02)00266-7.
[61] A. Houas, H. Lachheb, M. Ksibi, E. Elaloui, C. Guillard, J.M. Herrmann, Photocatalytic degradation pathway of methylene blue in water, Applied Catalysis B: Environmental. 31 (2001), https://doi.org/10.1016/S0926-3373(00)00276-9.
[62] S. Rajeshwari, J.S. Kumar, R.T. Rajendrakumar, N. Ponpandian, P. Thangadurai, Influence of Sn ion doping on the photocatalytic performance of V2O5 nanorods prepared by hydrothermal method, Mater. Res. Express 5 (2018) 25507, https://doi.org/10.1088/2053-1591/aaab0a.
[63] J. Su, X.-X. Zou, G.-D. Li, X. Wei, C. Yan, Y.-N. Wang, J. Zhao, L.-J. Zhou, J.-S. Chen, Macroporous V2O5−BiVO4 composites: effect of heterojunction on the behavior of photogenerated charges, J. Phys. Chem. C 115 (2011) 8064–8071, https://doi.org/10.1021/jp200274k.
[64] D. Rathore, S. Ghosh, J. Chowdhury, S. Pande, Co-doped Ni9S8 nanostructures for electrocatalytic water splitting over a wide pH range, ACS Appl. Nano Mater. 5 (2022) 11823–11838, https://doi.org/10.1021/acsanm.2c02842.
[65] D. Rathore, S. Ghosh, J. Chowdhury, S. Pande, Fe-doped NiCo2Se4 nanorod arrays as electrocatalysts for overall electrochemical water splitting, ACS Appl. Nano Mater. 6 (2023) 3095–3110, https://doi.org/10.1021/acsanm.3c00265.
[66] D. Rathore, S. Ghosh, A. Gupta, J. Chowdhury, S. Pande, Ce-doped NiSe nanosheets on carbon cloth for electrochemical water-splitting, ACS Appl. Nano Mater. 7 (2024) 9730–9744, https://doi.org/10.1021/acsanm.4c01607.
[67] J.-W. Rhim, B.-J. Yang, Singular flat bands, Adv. Phys. X. 6 (2021) 1901606, https://doi.org/10.1080/23746149.2021.1901606.
[68] M. Radecka, M. Rekas, A. Trenczek-Zajac, K. Zakrzewska, Importance of the band gap energy and flat band potential for application of modified TiO2 photoanodes in water photolysis, J. Power Sources 181 (2008) 46–55, https://doi.org/10.1016/j.jpowsour.2007.10.082.
[69] J. Wang, S.Y. Quek, Isolated flat bands and physics of mixed dimensions in a 2D covalent organic framework, Nanoscale 12 (2020) 20279–20286, https://doi.org/10.1039/D0NR04428H.